Driving forces of Ce(III) oxidation to Ce(IV) onto goethite

Gildas Ratié, K. Zhang, Muhammad Muqeet Iqbal, Delphine Vantelon, Fabrice Mahé, C. Rivard, M. Komárek, Martine Bouhnik-Le Coz, Aline Dia, K. Hanna, et al.

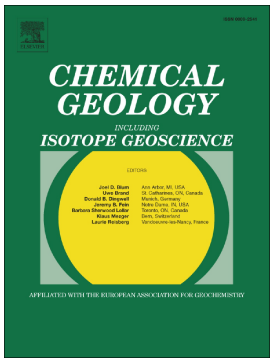

Driving forces of Ce(III) oxidation to Ce(IV) onto goethite

G. Ratié, K. Zhang, M. Iqbal, D. Vantelon, F. Mahé, C. Rivard, M. Komárek, M. Bouhnik-Le Coz, A. Dia, K. Hanna, M. Davranche, R. Marsac

PII: S0009-2541(23)00247-4

DOI: https://doi.org/10.1016/j.chemgeo.2023.121547

Reference: CHEMGE 121547

To appear in: *Chemical Geology*

Received date: 27 December 2022

Revised date: 12 April 2023

Accepted date: 10 May 2023

Please cite this article as: G. Ratié, K. Zhang, M. Iqbal, et al., Driving forces of Ce(III) oxidation to Ce(IV) onto goethite, *Chemical Geology* (2023), https://doi.org/10.1016/j.chemgeo.2023.121547

Driving forces of Ce(III) oxidation to Ce(IV) onto goethite

G. Ratié[1,2*], K. Zhang[3,4], M. Iqbal[3,5], D. Vantelon[6], F. Mahé[7], C. Rivard[6,8], M. Komárek[1], M. Bouhnik-Le Coz[3], A. Dia[3], K. Hanna[5], M. Davranche[3], R. Marsac[3*]

[1] *Department of Environmental Geosciences, Faculty of Environmental Sciences, Czech University of Life Sciences Prague, Kamýcká 129, 165 00, Prague – Suchdol, Czech Republic*

[2] *Univ. Orléans, CNRS, BRGM, ISTO, UMR 7327, F-45071, Orléans, France.*

[3] *Univ Rennes, CNRS, Géosciences Rennes - UMR 6118, F-35000 Rennes, France*

[4] *Department of Physics and Earth Sciences, Jacobs University Bremen, Campus Ring 1, 28759 Bremen, Germany*

[5] *Univ Rennes, École Nationale Supérieure de Chimie de Rennes, CNRS, ISCR – UMR6226, F-35000, Rennes, France*

[6] *SOLEIL Synchrotron, L'Orme des merisiers, Départementale 128, 91190 Saint Aubin, France*

[7] *Université de Rennes, CNRS, IRMAR - UMR 6625, F-35000, Rennes, France*

[8] *INRAE, TRANSFORM, UAR 1008, F-44316 Nantes, France*

*corresponding author: gildas.ratie@univ-orleans.fr; remi.marsac@cnrs.fr

Abstract

Iron (Fe) oxyhydroxides are major phases that may control the cerium (Ce) behavior in the Earth's Critical Zone. However, understanding Ce behavior with Fe oxyhydroxides remains uncompleted. Especially, if thermodynamic calculations suggest that Fe(III) is not a sufficiently strong oxidant, several studies reported the presence of Ce(IV) onto Fe oxyhydroxides. In this study, multiple approaches, including modeling and X-ray absorption spectroscopy, deciphered the driving forces of Ce(III) oxidation to Ce(IV) onto goethite. Results showed that oxidized Ce occurred onto goethite with a Ce(III)/Ce(IV) ratio depending on the Ce concentration in the solution ($[Ce]_{tot}$). The percentage of Ce(IV) onto goethite ranged from 20 % to 50 %, linearly increasing with $[Ce]_{tot}$. Comparable observation with a redox-inert Al-hydroxide (gibbsite), allowed to rule out the importance of Fe(III) redox reactivity as the main driver of Ce(III) oxidation. Instead, thermodynamic calculations suggested that surface precipitation of Ce(IV)-hydroxides, whose formation is favored with increasing $[Ce]_{tot}$, was an important driving force of the redox reaction. Because the goethite surface seemed to stabilize more strongly Ce(IV) than Ce(III) surface species than does gibbsite, differences in binding mechanisms of Ce(III) and Ce(IV) onto different mineral surfaces have been suggested to play a role on Ce redox speciation.

Keywords

Cerium, goethite, adsorption isotherms, redox, XANES Ce L_{III}-edge, speciation modeling.

1. Introduction

Rare Earth Elements (REE) are considered critical and strategic substances owing to their ever-increasing demand for many modern-day technologies (Massari and Ruberti, 2013; Ramos et al., 2016a). Their subsequent anthropogenic emissions make REE to be considered as emerging pollutants in the environment (e.g., Brioschi et al., 2013; Gwenzi et al., 2018; Kulaksız and Bau, 2011). Although their source and behavior in the Earth's mantle and crust are well characterized (Frey, 1984; Humphris, 1984; McLennan, 1989), many uncertainties persist due to the lack of studies related to the REE environmental mobility in the Earth's Critical Zone (Cao et al., 2001; Denys et al., 2021; Guénet et al., 2018; Ramos et al., 2016b).

Among REE, cerium (Ce) is the most abundant in the Earth's crust. Under oxic conditions, Ce can be oxidized as tetravalent Ce by adsorption-catalyzed oxidation (Bao and Zhao, 2008; Janots et al., 2015; Takahashi et al., 2000; Taylor and McLennan, 1988) controlled by oxidizing minerals, e.g., Mn or Fe oxyhydroxides (Davranche et al., 2005; Ohta and Kawabe, 2001; Takahashi et al., 2000), from precipitation in the liquid phase as $Ce(OH)_4$ or CeO_2 (Braun et al., 1990; De Baar et al., 1988; German and Elderfield, 1989; Marcus et al., 2018), and through specific biological processes (Kraemer et al., 2017; Moffett, 1990; Tanaka et al., 2010). The much larger affinity of Ce(IV) for surface, in regards to the other REE(III), makes it highly reactive to particles and colloids that subsequently control its mobility and transport (Liu et al., 2017; Marsac et al., 2013; Pédrot et al., 2015; Pourret et al., 2007b; Quinn et al., 2007). However, prediction of the Ce redox behavior is a challenging task because it is affected by several parameters and biogeochemical factors such as pH (Bau, 1999), the presence of colloids (Davranche et al., 2005; Pédrot et al., 2015; 2008), biotic activity (Ngwenya et al., 2009; Tanaka et al., 2010), and the organic matter (Gangloff et al., 2014; Pourret et al., 2007a).

The overall view of the REE behavior provides normalized REE patterns, which indicate a signature of their origin and geochemical processes (Henderson, 2013). In response to the behavior of its

trivalent neighbors (La and Pr), a positive or negative anomaly of Ce is observed and often highlights changes in O_2 availability due to the redox-sensitivity of Ce as compared with other REE. Because of this peculiar redox sensitivity, Ce anomalies have, therefore, often been considered as efficient paleo-redox tracers in many environments (Nakada et al., 2013a; Shields and Stille, 2001; Tostevin et al., 2016; Tostevin, 2021; Zhong et al., 2019). The positive Ce anomaly associated to Ce(IV) adsorbed to MnO_2 is well-known and documented (e.g., Loges et al., 2012; Nakada et al., 2013b; Takahashi et al., 2007). Thermodynamic data show that the $Mn^{2+}/Mn(IV)O_2$ standard potential (E^0) is higher than the E^0 of $Ce^{3+}/Ce(IV)O_2$ (Brookins, 2018); namely that Mn(IV) is reduced as Mn(III) or Mn(II) by oxidizing Ce(III) to Ce(IV) (Ohta and Kawabe, 2001). The oxidative pathway of Ce by MnO_2 corresponds to the Ce(III) adsorption followed by its oxidation as Ce(IV) and preferential adsorption relative to the REE(III) (Ohta and Kawabe, 2001) or as $Ce(OH)_4$ nanoparticles (Nakada et al., 2017). On the contrary, for Fe oxyhydroxides, the electron transfer should not occur because the E^0 of $Fe^{2+}/Fe(III)$-(oxy)(hydr)oxides is significantly lower than that of $Ce^{3+}/Ce(IV)O_2$ (Stumm and Sulzberger, 1992). However, contrasted results were obtained, such as (i) low Ce oxidation at acidic pH onto hydrous Fe oxide (Bau, 1999), (ii) Ce(IV) adsorption and incorporation to hematite (Bolanz et al., 2018; Takahashi et al., 2002), (iii) total Ce oxidation onto goethite (Yu et al., 2017) or (iv) partial Ce oxidation onto goethite (Denys et al., 2021; Ratié et al., 2020). These results evidence the lack of knowledge about the behavior of Ce oxidation processes in contact with Fe oxyhydroxides. Several mechanisms might be invoked to explain these discrepancies, such as the crystalline structure of the Fe -oxyhydroxides and their synthetic or natural origin, or the redox condition during the interaction of Ce with Fe oxyhydroxides. In addition, thermodynamic aspects at mineral-water interfaces have also been shown for plutonium (Pu), a chemical analogue of Ce. Previous studies revealed that Pu(IV) was more stabilized at clays surfaces than Pu(III). This process highly depended on the Pu-clay binding mechanisms, i.e., surface complexation, cation exchange or surface precipitation (Banik et al., 2016; Marsac et al., 2015a; 2017a).

Up to now, no systematic study of Ce interaction with a single Fe oxyhydroxide has been conducted, which would allow deciphering the reason for the occurrence of Ce(IV) at the Fe

oxyhydroxide surface. Therefore, to quantitively observe the adsorption or precipitation processes responsible for the Ce(IV) bound onto goethite, this study combined isotherm adsorption experiments, numerical modeling, and X-ray absorption spectroscopy focusing on the XANES (X-ray Absorption Near Edge Structure) Ce L_{III}-edge spectrum. To identify the redox control potentially exerted on the Ce adsorption by goethite, a trivalent analog non-redox-sensitive REE, namely Nd, was also studied. Moreover, to compare the role of goethite surface on the Ce redox behavior, we also performed Ce batch experiments to gibbsite, i.e., inert redox surface. Using this approach, we determined the mechanism behind the Ce(III)/Ce(IV) ratio occurring at the goethite surface, allowing us to explain the different results yet published.

2. Materials and Methods

All chemicals used were of analytical grade. All experimental solutions were prepared with double-deionized water (Milli-Q system, Millipore™). Synthetic Ce and Nd solutions were prepared from nitrate Ce and Nd standard solutions (10 g L^{-1}, in 5% HNO_3, AccuTrace™ Reference Standard). Polyethylene containers were all soaked in 10% Ultrapure HNO_3 for 48 h at 60°C, then rinsed with deionized water for 24 h at 60°C to remove all contamination sources.

2.1. Batch experiments

2.1.1. Preparation of goethite and gibbsite

A goethite suspension was prepared by neutralizing a volume of 500 mL of 0.5 mol L^{-1} ferric $Fe(NO_3)_3 \cdot 9H_2O$ solution with a 400 mL 2.5 mol L^{-1} NaOH solution added at a rate of 1 mL min^{-1} (Hiemstra et al., 1989). The solution was stirred vigorously during the NaOH addition in a glove box (N_2). The precipitate was aged for 72 h at 60 °C. The final suspension was dialyzed at 1 kDa (Spectra/Por membrane 2) with Milli-Q water. The water was changed twice a day until the suspension conductivity was close to 0 µS cm^{-1}. The dialyzed suspensions were stored in polypropylene containers at 4°C. An aliquot of the dialyzed suspension was dried at 60 °C for 24h. X-Ray Diffractogram was recorded on the

dry powders to confirm the synthesis of goethite. The Brunauer-Emmett-Teller (BET) specific surface area of the synthesized goethite was 81 $m^2 g^{-1,}$ and the point of zero charge (PZC) was estimated at 9.1 by potentiometric titration (Cheng et al., 2019). Transmission electron microscopy (TEM, Jeol JEM 1230 microscope) images showed goethite needle particles of around 100 nm long (Figure S1). Gibbsite ($Al(OH)_3$) was synthesized as described in (Jodin et al., 2005). The BET specific surface area of the synthesized gibbsite was 20 $m^2 g^{-1,}$ and the PZC was estimated at 9.8.

2.1.2. Adsorption isotherms

All adsorption isotherm experiments were performed under ambient air, at room temperature, i.e., 20°C ± 2. Adsorption experiments of Ce and Nd (noted "Ce/Nd" in the following text) by goethite and gibbsite were carried out using 0.5 g L^{-1} of goethite and 2 g L^{-1} of gibbsite in 5 mM NaCl solution. The ratio between gibbsite and goethite depends on their BET specific surface. The range of $[Ce/Nd]_{tot}$ varied from 250 to 5000 µg L^{-1}, noted Ce/Nd250 to Ce/Nd5000. Such concentrations were selected in response to the necessary concentration for XANES investigations. The pH was adjusted to pH 6 (e.g., pH conditions commonly encountered in soils) and monitored over time using 0.1 M NaOH/HCl solution (Hach, sensION+). The Ce/Nd-goethite and gibbsite suspensions were stirred for 24 h, as it is often considered as a sufficient equilibration time in adsorption experiments. Additionally, an aliquot was maintained under stirring for 70 days for Ce-goethite suspension to check potentially slow kinetic processes. The remaining suspension was centrifuged at 3000 g for 30 min. The resulting centrifuge was air dried and stored at room temperature for XANES investigations. The solution was filtered at 0.2µm (PES filter, Sartorius), acidified to 2% HNO_3 for Ce/Nd concentration analysis ($[Ce/Nd]_{aq}$), determined by Quadruple ICP-MS using an Agilent Technologies 7700×. Concentrations of Fe and Al were also monitored, and the low values confirmed that the amounts of goethite and gibbsite were negligible in the filtrate, as previously expected or determined in previous comparable studies (Cheng et al., 2019; Luo et al., 2022; Xu et al., 2017).

2.2. Cerium L_{III}-edge XANES investigation

Using Ce L_{III}-edge XANES spectra allows for identifying the oxidation states +III and +IV of Ce through their different electron transitions during measurement. Overall, the Ce(III) model compounds express a white line corresponding to the $2p_{3/2} \rightarrow (4f^1)5d$ transition, while the Ce(IV) model compounds exhibit a white line with two maxima because of the mixed-valence behavior of tetravalent Ce in its final state, due to the interaction between 4f orbitals of the Ce and 2p orbitals of the O ligand in its initial state (Malterre, 1991). This corresponds to two electronic transitions: the lower-energy peak is assigned to the $2p \rightarrow 5d$ transition with $4f^1\underline{L}$ configuration, and the higher-energy peak is assigned to the $2p \rightarrow 5d$ transition with $4f^0\underline{L}$ configuration (Fonda et al., 1999; Soldatov et al., 1994).

2.2.1. XANES acquisition

X-ray absorption experiments were performed on the LUCIA beamline (SOLEIL synchrotron) (Flank et al., 2006; Vantelon et al., 2016). The X-ray beam was monochromatized using a Si (111) double-crystal monochromator. The monochromator was calibrated by setting the first inflection point of a Cr metallic foil XANES spectrum to 5927 eV. Spectra were collected in fluorescence mode (using a Bruker 60 mm^2 mono-element SDD). Cerium L_{III}-edge XANES spectra were collected with a beam size of 2*2 mm^2 under a secondary vacuum (10^{-7} mbar) and at 25 K, using a liquid He cryostat. A set of spectra published by Ratié et al. (2020) were used for reference compounds ($CePO_4$, $Ce(NO_3)_3.6H_2O$, $Ce(OH)_4$, $Ce(SO_4)_2$, Ce-doped δMnO_2 and humic acid).

The Ce-goethite samples were prepared as pellets of finely ground and homogenized powder mixed with cellulose. Measures were performed using the XANES "e-flyscan" continuous mode available on the LUCIA beamline, ranging from 5680 eV to 5800 eV with an energy step of 0.4 eV and a counting time of 300 ms per point. The recorded spectra (up to ten) were superimposable for each sample, confirming that no beam damage occurred during measurements and then merged. XANES spectra were processed using the Athena software (Ravel and Newville, 2005). Normalized spectra were obtained by

fitting the pre-edge region with a linear function and the post-edge region with a quadratic polynomial function.

2.2.2. Cerium solid speciation

The Ce speciation in the studied sample can be obtained by Linear Combination Fits (LCF) of Ce references XANES spectra. However, for an identical valence, with Ce in different phases, the XANES spectrum does not allow to identify slight different structures (Chalmin et al., 2009; Farges, 2005). An alternative method exists to focus on the valence state instead of the Ce speciation for allowing the determination of the Ce(III)/Ce(IV) ratio: linear combinations with a database of pure-valence species (the Combo method), already applied for determining Mn valence states (Manceau et al., 2012). For applying to Ce valence states, that method consists in performing LCF with several known Ce valence reference compounds. The attribution to the Ce(III) state is considered as the sum of fractions of each Ce(III) species in the fit and the same for Ce(IV) state for estimating the Ce(III)/Ce(IV) ratio in the goethite samples.

Linear CF were performed on the normalized and first derivative of Ce L_{III}-edge spectra from 5700 eV to 5743 eV, to avoid any influence of the first oscillations depending on the coordination sphere Ce-O of each structure of references, and not forcing the weights to sum up to 1, using the Athena software (Ravel and Newville, 2005). The R-factor and the χ^2 reduced were used to characterize the LCF accuracy. The precision of the LCF-XANES approach, by fitting mechanically-mixed Ce reference compounds, is approximately 10% (Janots et al., 2015; Takahashi et al., 2002).

2.2.3. Iterative algorithm

Additionally, if references XANES spectra of Ce(III) and Ce(IV) compounds are not known *a priori* to be used in LCF, another way to determine the Ce(III)/Ce(IV) is to use an optimization algorithm to minimize the difference between the measurement results and the results of the following decomposition:

$$A(E, [Ce]_{tot}) = f_1([Ce]_{tot}) \times A_1(E) + (1 - f_1([Ce]_{tot})) \times A_2(E) \qquad (1)$$

Where *A* values are calculated normalized XANES intensities, f_1, A_1, and A_2 are the variables to be determined, which correspond to the fraction of Ce(IV), the normalized XANES intensities of pure Ce(IV) and Ce(III) compounds, respectively. The deviation function to be minimized can be written as:

$$J(f_1, A_1, A_2) = \sum_{i=1}^{n} \sum_{j=1}^{m} \left(A(E_i, [Ce]_{tot,i}) - A\_meas(E_i, [Ce]_{tot,i}) \right)^2 \quad (2)$$

where, *n* is the number of energies E_i and *m* is the number of concentrations $[Ce]_{tot,i}$ used for the measurements, and *A_meas* is the measured XANES intensity. To solve this optimization problem, an iterative two-step method is used: A_1 and A_2 are determined assuming that f_1 is fixed, then f_1 is determined assuming that A_1 and A_2 are fixed, and the process is repeated until convergence. f_1 is initialized to values regularly spaced from 0.2 to 0.5, A_1(E) is initialized to A_meas for $[Ce]_{tot}$=5000 µg L^{-1}, and A_2(E) to A_meas for $[Ce]_{tot}$=250 µg L^{-1}. The Sequential Quadratic Programming (Nocedal and Wright, 2006) method is used to solve each of the internal optimization problems with the Matlab™ software.

2.2.4. Geochemical speciation modeling

Predominance (pH-Eh) diagrams were obtained using PhreePlot (Kinniburgh and Cooper, 2011), which contains an embedded version of the speciation code PHREEQC (Parkhurst and Appelo, 2013). Aqueous Ce(III) and Ce(IV) reactions and equilibrium constants were taken from (Marsac et al., 2017b). The Davies equation was used to extrapolate thermodynamic constants at various ionic strengths.

3. Results and discussion

3.1. Neodymium and cerium adsorption to goethite and gibbsite

Neodymium adsorption isotherm to goethite reached a plateau at around 19 µg m^{-2} (Figure 1a). This behavior was fitted using a Langmuir isotherm model:

$$[Nd]_{ads} = Q_{max,Nd} \frac{(K_{Nd}[Nd]_{aq})}{1+(K_{Nd}[Nd]_{aq})} \quad (3)$$

where, $Q_{max,Nd}$ is the maximum amount of adsorbed Nd (µg m^{-2}), and K_{Nd} is the Langmuir constant. All parameters were determined by a least-square fit (Table 1). By contrast, the amount of adsorbed Ce

constantly increased to reach 30 µg m^{-2} at the highest $[Ce]_{tot}$ (5000 µg L^{-1}), and no plateau was reached. The concentration of adsorbed Ce overpassed that of Nd for $[Ce/Nd]_{aq}$ = 1400 µg L^{-1} (i.e. $[Ce/Nd]_{tot}$ = 2000 µg L^{-1}). At low $[Ce/Nd]_{aq}$, the highest adsorption is expected for Nd than for Ce because Nd is bound more strongly by ligands (including surface -OH groups) than Ce (Davranche et al., 2004; Ohta and Kawabe, 2001; Quinn et al., 2004), because of their hydrolysis constants (Brown and Ekberg, 2016; Rizkalla and Choppin, 1994). At high $[Ce/Nd]_{aq}$, Ce is more adsorbed than Nd in response to the incomplete oxidation of Ce(III) to Ce(IV), which is more adsorbed than Ce(III) by mineral surface (Bau, 1999; Ohta and Kawabe, 2001; Takahashi et al., 2007, 2000). Interestingly, this oxidation seems fast since Ce adsorption equilibrium was reached at around 24h and did not evolve until 70 days (Figure 1a).

Table 1: Experimental results of Nd and Ce sorption onto goethite and parameters used for modeling Nd and Ce sorption onto goethite surfaces, as well as the Ce(III)/Ce(IV) adsorbed ratio.

Goethite	Experiment results			Modeling parameters			Modeling results		
Sample name	$[\ ]_{total}$ µg L^{-1}	$[\ ]_{aq}$ µg L^{-1}	$[\ ]_{ads}$ µg m^{-2}		Nd	Ce	$[\ ]_{ads}$ µmol m^{-2}	$[Ce(III)]_{ads}$ µg m^{-2}	$[Ce(IV)]_{ads}$ µg m^{-2}
	Nd (1 day)			Qmax (µg m^{-2})	19.87	19.31	Nd (1 day)		
Nd250	253	61	4.8	logKads	-2.40	-3.01	3.9		
Nd500	505	177	8.2	m	1.00	1.00	8.2		
Nd750	746	312	10.9	logKpoly	-	-0.04	11.0		
Nd1000	1049	532	12.9	n	-	0.87	13.5		
Nd2000	2070	1376	17.4				16.8		
Nd3000	3006	2269	18.4				17.9		
Nd5000	5219	4479	18.5				18.8		
	Ce (1 day)						Ce (1 day)		
Ce250	252	79	4.3				1.9	1.4	0.5
Ce500	496	231	6.6				4.8	3.5	1.3
Ce750	749	451	7.5				8.2	5.9	2.3
Ce1000	988	591	9.9				9.9	7.1	2.9
Ce2000	2075	1398	16.9				17.2	11.1	6.1
Ce3000	3223	2202	25.5				22.2	13.2	9.0
Ce5000	5116	3913	30.1				30.1	15.3	14.8
	Ce (70 days)								
Ce250	252	77	4.358						
Ce500	496	227	6.726						
Ce750	749	445	7.600						
Ce1000	988	613	9.363						
Ce2000	2075	1396	16.967						
Ce3000	3223	2160	26.558						
Ce5000	5116	3865	31.267						

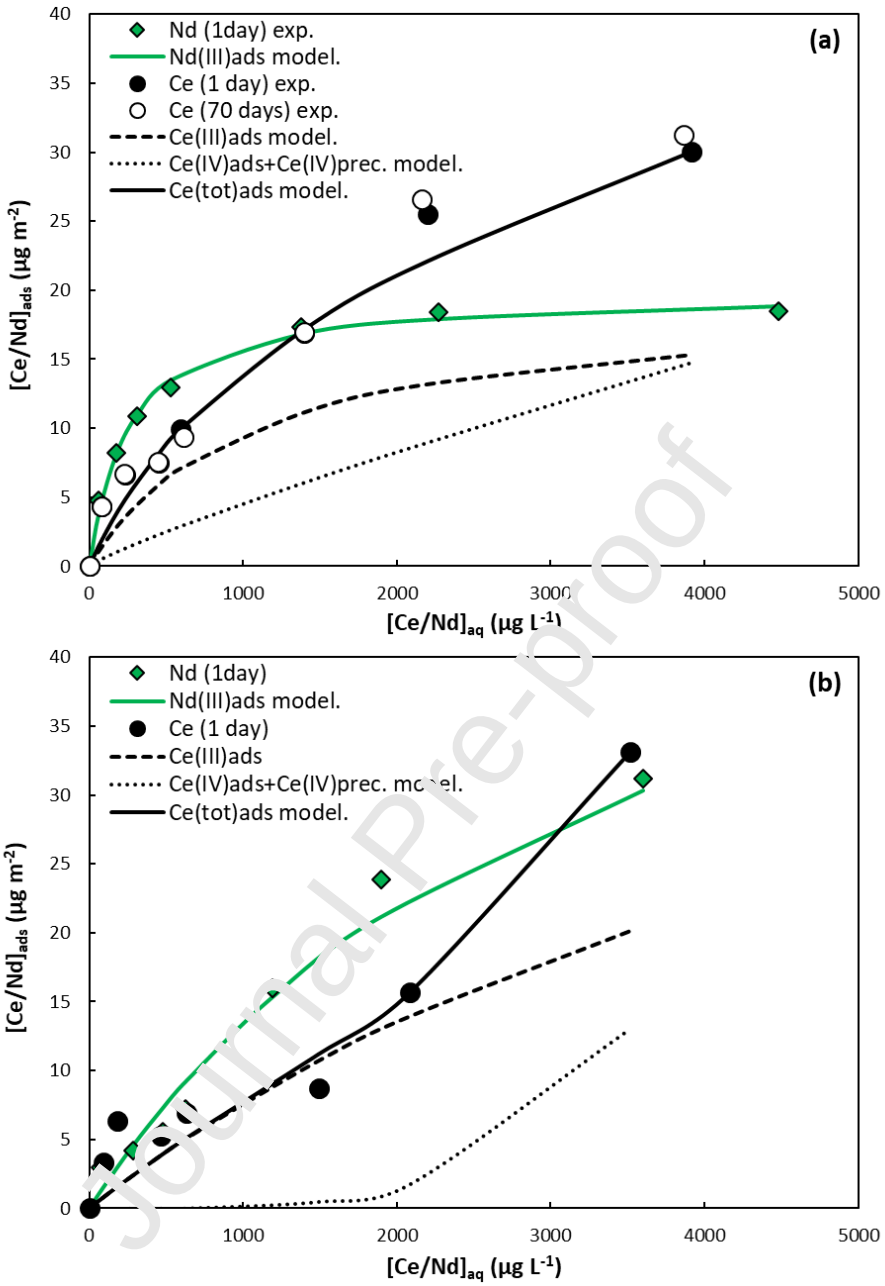

Figure 1*: Nd and Ce adsorption isotherms onto (a) goethite (0.5 g L^{-1}) and (b) gibbsite (2 g L^{-1}), at pH 6 in 5 mM NaCl. Experimental data (exp.) are represented by circles, whereas modeled data are displayed as lines. The green line represents the adsorbed Nd(III) using the Langmuir model, and the black line corresponds to the sum of adsorbed Ce(III) (black dashed line) calculated with the Langmuir model and the adsorbed Ce(IV) and/or Ce(IV) surface precipitation (black dotted line) calculated with a Freundlich model.*

The difference between Nd and Ce adsorption isotherm suggests different adsorption processes. A unique Langmuir isotherm did not succeed in fitting Ce adsorption by goethite. An additional Freundlich isotherm had to be used to consider the oxidation of Ce(III) as Ce(IV):

$$[Ce]_{ads} = Q_{max,Ce}\frac{(K_{Ce}[Ce]_{aq})}{1+(K_{Ce}[Ce]_{aq})} + \left(K_{poly}[Ce]_{aq}\right)^{n} \quad (4)$$

Where, $Q_{max,Ce}$ is the maximum amount of adsorbed Ce (µg m^{-2}), K_{Ce} is the adsorption constant, K_{Poly} the Freundlich constant, and n is the non-linear parameter. A similar model was previously used for silicate binding and polymerization/precipitation onto Fe oxyhydroxides (Kamenetsu et al., 2018). By assuming that (i) the maximal binding capacity is the same for Nd and Ce(III) ($Q_{max,Ce} = Q_{max,Nd}$, when expressed in mol m^{-2}) and that (ii) Ce(III) and Nd(III) are adsorbed on the same surface sites, the values of K_{Ce}, K_{Poly}, and n can be determined by a least-square fit. This model allowed us to reproduce the experimental datasets with a RMSE = 0.033. This model will be further used to discuss the Ce redox speciation in combination with XANES results.

Neodynium adsorption isotherm followed the same trend as the gibbsite (Figure 1b). The Langmuir isotherm model allowed us to reproduce the Nd adsorption datasets (Eq. 3) (Table 2). A larger binding capacity but a smaller Langmuir constant were calculated for gibbsite than for goethite. At low $[Ce]_{tot}$ concentration, the Ce adsorption was smaller than that of Nd, but was higher at the highest $[Ce]_{tot}$ concentration. Cerium adsorption isotherm has also been fitted by a combination of Langmuir and Freundlich isotherms, RMSE = 0.045 (Eq. 4). Figure 1b exhibits the contribution of Ce(III) and Ce(IV) adsorption onto gibbsite, respectively. Cerium(III)/Ce(IV) adsorption onto the mineral depends on the Ce concentration in the solution and the mineral that controls the Ce redox equilibrium.

Table 2: Experimental results of Nd and Ce sorption onto gibbsite and parameters used for modeling Nd and Ce sorption onto gibbsite surfaces, as well as the Ce(III)/Ce(IV) adsorbed ratio.

Gibbsite	Experiment results			Modeling parameters			Modeling results		
Sample name	$[\ ]_{total}$ µg L^{-1}	$[\ ]_{aq}$ µg L^{-1}	$[\ ]_{ads}$ µg m^{-2}		Nd	Ce	$[\ ]_{ads}$ µmol m^{-2}	$[Ce(III)]_{ads}$ µg m^{-2}	$[Ce(IV)]_{ads}$ µg m^{-2}
	Nd (1 day)			Qmax (µg m^{-2})	58.70	57.02	Nd (1 day)		
Nd250	206	75	3.0	logKads	-3.53	-3.81	1.3		
Nd500	465	282	4.2	m	1.00	1.00	4.5		
Nd750	702	479	5.5	logKpoly	-	1.91	7.3		
Nd1000	942	628	7.2	n	-	3.33	9.2		
Nd2000	1886	1188	16.0				15.3		
Nd3000	2875	1899	23.9				21.2		
Nd5000	4887	3601	31.2				30.3		
	Ce (1 day)						Ce (1 day)		
Ce250	229	90	3.3				0.8	0.8	0.0
Ce500	459	185	6.3				1.6	1.6	0.0
Ce750	678	465	5.3				3.8	3.8	0.0
Ce1000	926	635	6.9				5.1	5.1	0.0
Ce2000	1841	1431	8.7				11.2	10.7	0.5
Ce3000	2748	2087	15.7				15.7	13.9	1.8
Ce5000	4865	3518	33.1				33.1	20.1	13.0

3.2. Cerium solid speciation

3.2.1. XANES of Ce references

The Ce(III) references displayed Ce L_{III}-edge XANES spectra with an intense white line at 5726 eV, followed by a broad oscillation centered around 5755-5760 eV (Figure 2a). The Ce(IV) references showed a white line with two maxima, followed by a broad oscillation centered at 5773 eV. According to the different Ce(IV) references, the first maximum ranged from 5729 eV to 5731 eV, and the second maximum from 5737 eV to 5738 eV. The differences in intensity and position between the first two maxima of the Ce(IV) species are explained by changes in covalent character in the Ce-O bond (Kaindl et al., 1988). Additionally, the first derivative of the spectra was also expressed to reveal the valence state of transition without the effect of coordination and symmetry (Figure 2b). The Ce(IV) references derivative spectra exhibited peaks at 5725 eV and 5735 eV that can be assigned to the +IV electronic state, while the Ce(III) references indicated a peak at 5724 eV that can be assigned to the +III electronic state.

3.2.2. Goethite-Ce samples

The Ce L_{III}-edge XANES spectra of the goethite samples exhibited a singular white line at 5726 eV, matching the Ce(III) references (Figure 3). The intensity of the white line decreased from sample Ce250 to sample Ce5000. This decrease is coupled with the increase of a shoulder at 5737 eV, matching with the second maximum of the Ce(IV) references spectra, which intensity increased from sample Ce250 to sample Ce5000. The XANES spectra exhibited three isosbestic points indicating that Ce speciation can be described using solely two Ce phases or a set of Ce phases whose proportions do not vary (Figure 3).

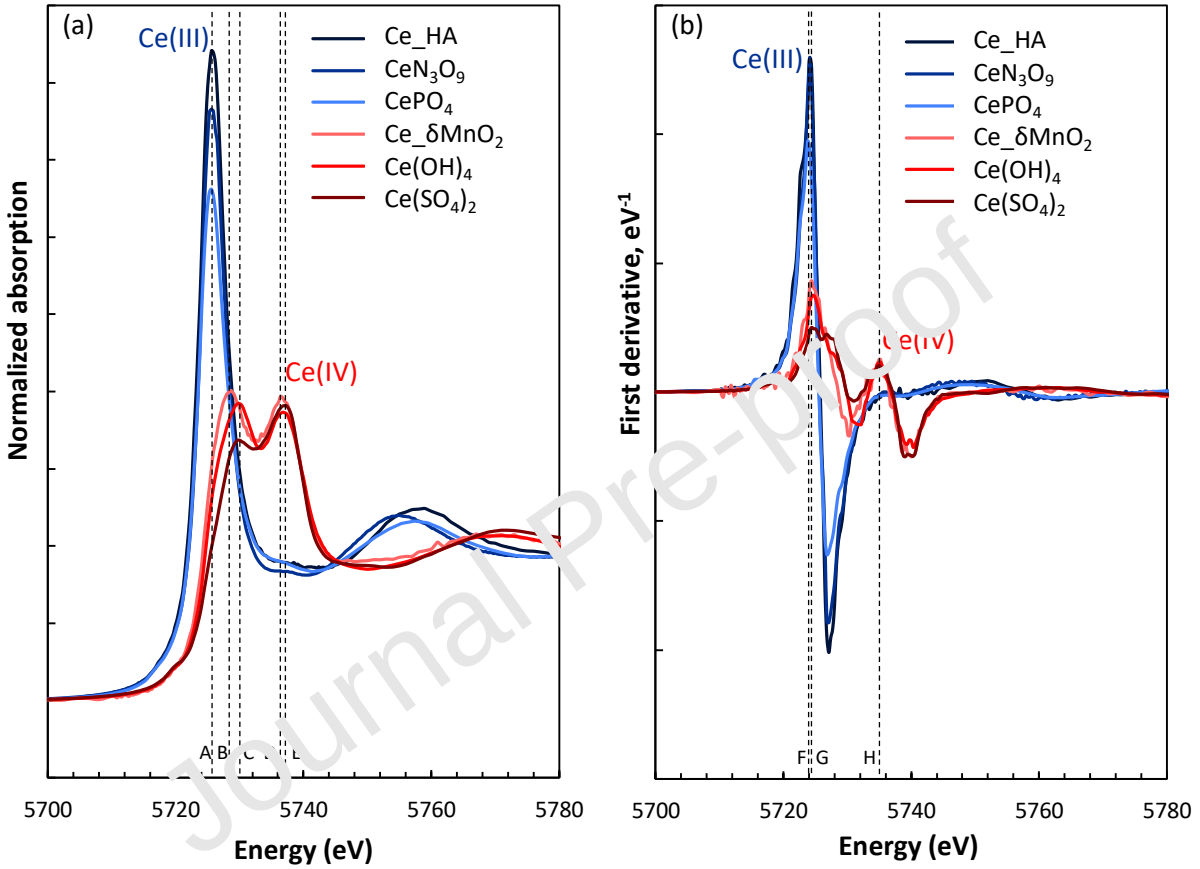

Figure 2: *Ce L_{III}-edge XANES absorption normalized spectra (a) and first derivatives spectra (b) of single-valent Ce(III) (solid blue lines) and Ce(IV) (solid reddish lines) species. Peaks A, B, C, D, and E correspond to 5726 eV, 5729 eV, 5731 eV, 5737 eV, and 5738 eV, respectively. Peaks F, G, and H correspond to 5724 eV, 5725 eV, and 5735 eV, respectively. Ce_HA means Ce adsorbed to humic acid.*

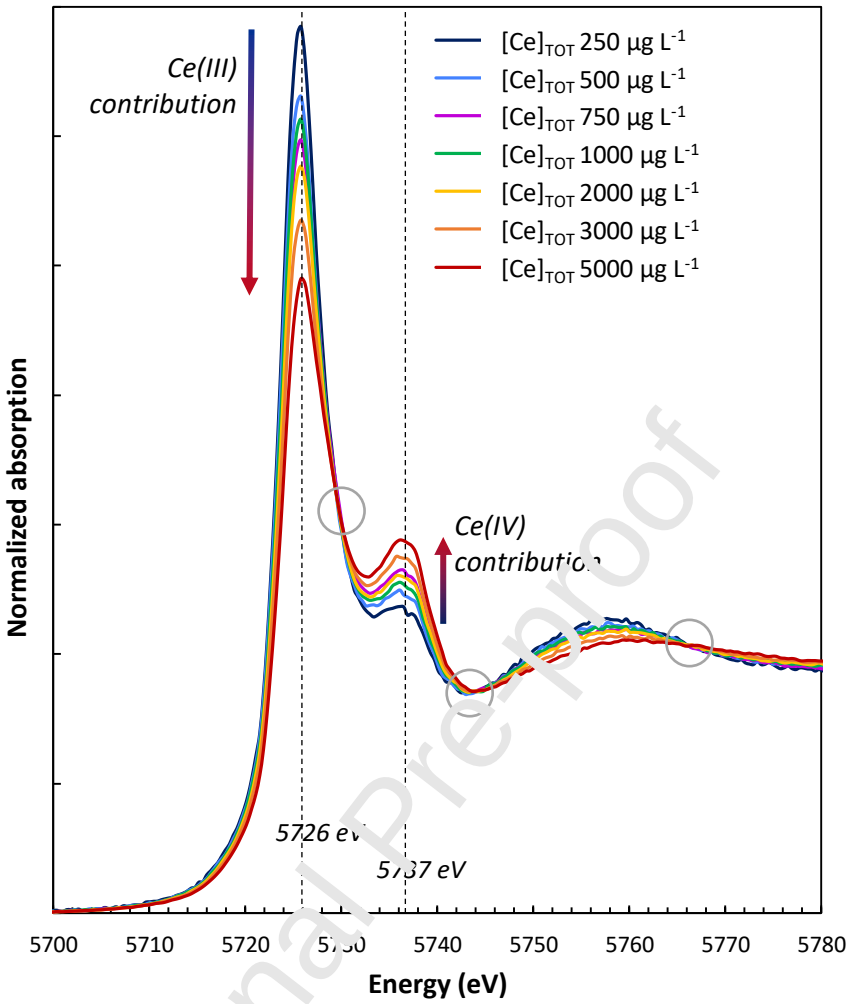

***Figure 3**: Ce L_{III}-edge XANES absorption normalized spectra of the goethite samples. The arrows represent the Ce oxidation state, i.e., lower Ce(III) and higher Ce(IV) contributions, as a function of the increasing Ce concentration in the solution. The dashed grey circles highlight the isosbestic points. $[Ce]_{TOT}$ corresponds to the initial concentration of Ce in the solution.*

3.2.3. Ce(III)/Ce(IV) ratios

The normalized and first derivative Ce L_{III}-edge XANES were deconvoluted using the Combo method (Figure S2). As previously described, first derivative spectra allow focusing on the oxidation state instead of the crystalline structure. Both results were compared, and the numerical results of LCF are reported in Table S1. The reduced χ^2 used to characterize the quality of the fit varies from 1 10^{-3} to 5 10^{-4} for normalized spectra, allowing us to discuss the Ce(III)/Ce(IV) ratios in the goethite samples.

The contribution of Ce(III) resulted from the contribution of $CePO_4$, and Ce(III) adsorbed to humic acid, while the Ce(IV) contribution resulted from the contribution of $Ce(SO_4)_2$ and Ce(IV) adsorbed to δMnO_2 (Table S1). The Ce(III)/Ce(IV) ratio oxidation state progressively increased relative to the initial Ce concentration in the solution (Table S1). From Ce250 to Ce5000, Ce(IV) ranged from 21% to 49% for normalized spectra and from 20% to 48% for first derivative spectra. The homogeneous results between normalized spectra and first derivative spectra LCF highlighted the negligible influence of the variation of the normalized spectra of Ce(IV) references for LCF, considering the analytical error of LCF, estimated to ± 10%.

As a complementary approach using an iterative algorithm based only on Ce L_{III}-edge XANES absorption normalized spectra determined the normalized intensities of components Ce(III) and Ce(IV) (Figure S3). This allowed estimating the Ce(IV) contribution. From Ce250 to Ce5000, Ce(IV) ranged from 19% to 53% (Table S1).

Both LCF and the iterative algorithm provided consistent results showing that the Ce(IV) amount increased proportionally with the Ce concentration in the solution (Figure 4). At the lowest Ce concentration ($[Ce]_{tot}$ = 250 µg L^{-1}), the Ce(IV) proportion represented ≈ 20 % of the total adsorbed Ce, whereas at the highest Ce concentration ($[Ce]_{tot}$ = 5000 µg L^{-1}), the Ce(IV) proportion reached ≈ 50%. These results are in good agreement with the modeling approach assuming that the Langmuir (left member of eq.2) and Freundlich (right member of eq.2) isotherms correspond to the uptake of Ce(III) and Ce(IV) by goethite, respectively (Figure 4).

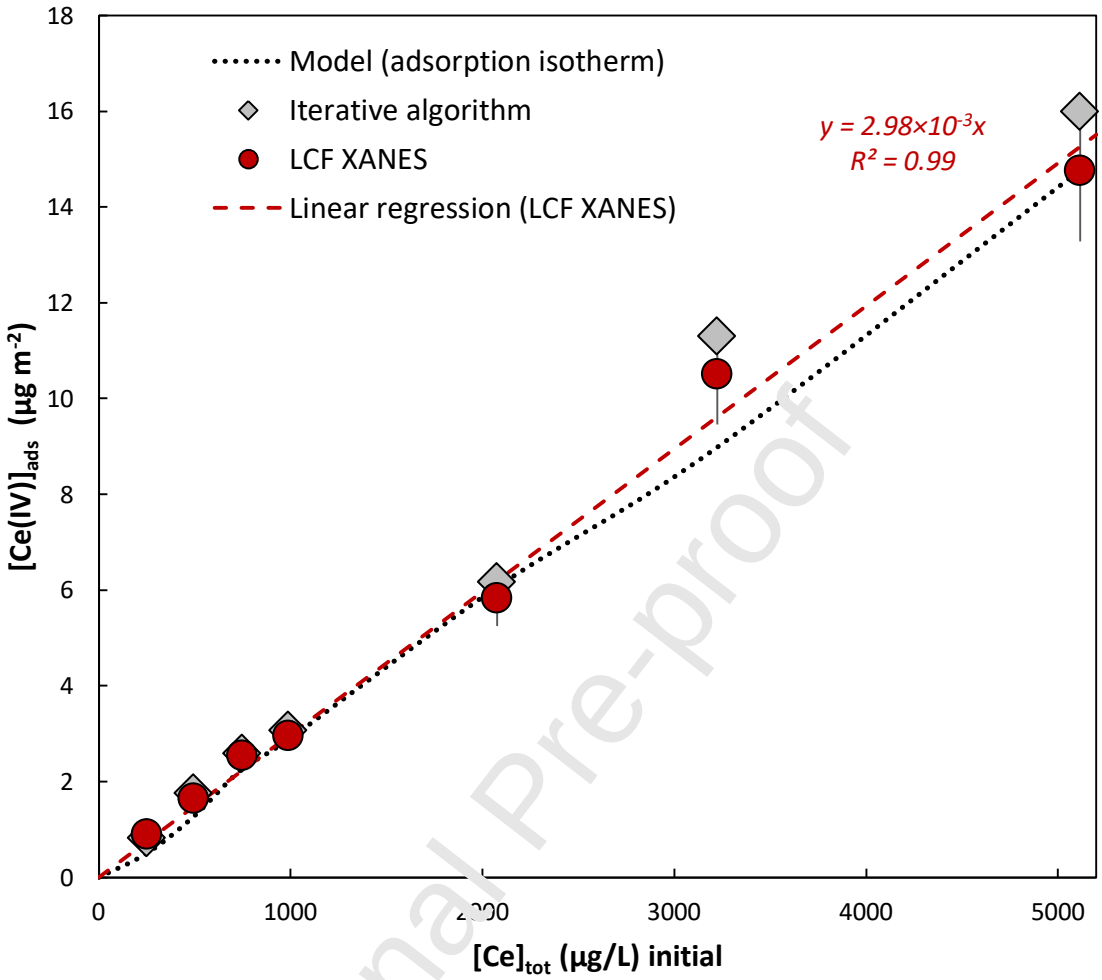

Figure 4*: Comparison between the $[Ce(IV)]_{ads}$ determined from XANES spectra (LCF and iterative algorithm) and by the model (adsorption isotherm) as a function of the initial Ce concentration in solution. The dotted dash line represents the linear regression of the $[Ce(IV)]_{ads}$ (LCF XANES) as a function of the $[Ce]_{tot}$ in solution. The error bar for LCF is considered as ± 10%.*

3.3. Thermodynamic aspects

Interpretation of Nd and Ce adsorption isotherms onto goethite evidenced the incomplete oxidation of Ce(III) to Ce(IV), which was confirmed by XANES results on goethite. That result suggests, at first glance, the possible role of Fe(III) for Ce oxidation to goethite surface, as very often observed in the presence of MnO_2. However, by contrast with the Mn(II)/MnO_2 redox couple, the Fe(II)/goethite redox potential is significantly lower than that of Ce(III)/Ce(IV) (Stumm and Sulzberger, 1992). In

addition, the formation of Ce(IV) in the presence of gibbsite, which is redox-inert, shows that the mineral oxidizing capacity is not the only driving process in the oxidation of Ce(III) to Ce(IV).

A linear relationship exists between $[Ce(IV)]_{goe}$ and the total concentration of Ce in the goethite suspension (Figure 4). Cerium(IV) contribution is, therefore, rather related to the solution saturation than to a redox surface effect. The redox stability range of Ce(IV) increases with the increasing total Ce concentration, as can be observed on the pH-E_H predominance diagram (Figure 5a) in response to the Ce(IV)-mineral formation. Amorphous $Ce(OH)_{4(am)}$ is rather expected than crystalline $CeO_{2(s)}$ (Marsac et al., 2017b; Neck et al., 2003; Neck and Kim, 2001), according to the following half-reaction:

$$Ce^{3+} + 4H_2O \rightleftharpoons Ce(OH)_{4(s)} + 4H^+ + e^- \quad (5)$$

Similarly, the apparent (i.e., concentration dependent) redox potential of the prevailing Ce(IV)/Ce(III) species ($E'_{Ce(IV)/Ce(III)}$) can be calculated both in the aqueous and solid phases of the suspension, that correspond to the Ce(IV)-Ce(III) borderline of the Pourbaix diagram at pH = 6 (Figure 5b). Values of $E'_{Ce(IV)/Ce(III)}$ remained constant at low $[Ce]_{tot}$ because no precipitation occurred, hence equal to the apparent redox potential of the $Ce(OH)_3^+/Ce^{3+}$ at pH = 6 in 5×10^{-3} M NaCl. When $[Ce]_{tot}$ increased, $E'_{Ce(IV)/Ce(III)}$ decreased because of the formation of $Ce(OH)_{4(am)}$. If we assume that the experimental redox potential (E_H) is independent of the $[Ce]_{tot}$, since controlled by atmospheric O_2, we can conclude that Ce(III) oxidation to Ce(IV) is promoted when $[Ce]_{tot}$ increases. This explains the present and the opposite results in the literature at high and low $[Ce]_{tot}$ (Ratié et al., 2020; Yu et al., 2017).

If $Ce(OH)_{4(am)}$ precipitation explains the increasing thermodynamic stability of Ce(IV) over Ce(III) for increasing $[Ce]_{tot}$, it does not fully explain all the present datasets. Cerium(IV) was observed onto goethite at the lowest $[Ce]_{tot}$, whereas Ce(IV) was expected to occur in a significant amount onto gibbsite for the highest $[Ce]_{tot}$. The binding mechanisms of Ce(III) and Ce(IV) onto different minerals might thus control the Ce redox speciation at equilibrium. Previous studies revealed that the redox speciation of actinides (Np and Pu) was affected by clay surfaces presenting different affinities for two

distinct oxidation states (e.g., Pu(III) and Pu(IV)) (Banik et al., 2017, 2016; Marsac et al., 2017a, 2015a, 2015b). Accordingly, goethite stabilizes more strongly Ce(IV) than gibbsite.

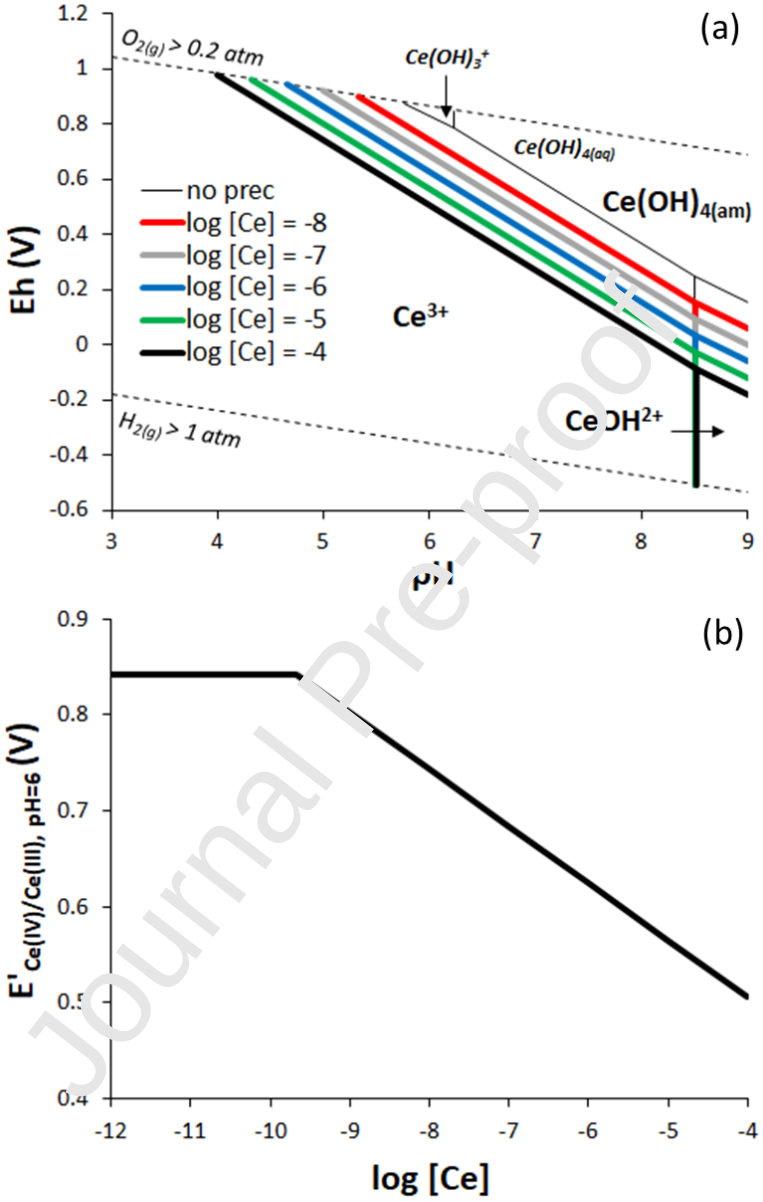

Figure 5: (a) Eh-pH diagram for Ce in 5 × 10^{-3} M NaCl solution accounting or not for the precipitation of $Ce(OH)_4$(am), as a function of total Ce concentration. (b) The apparent redox potential of the prevailing Ce(IV)/Ce(III) species (E'Ce(IV)/Ce(III)) in the suspension (i.e., both in the aqueous and solid phases) at pH = 6 (that of the adsorption isotherms).

4. Conclusions

This study provided adsorption datasets of Nd and Ce sorption onto goethite and gibbsite. Fitting the datasets of both goethite (oxidative surface) and gibbsite (non-redox sensitive surface) with a combined Langmuir and Freundlich model, we conclude that Fe(III) redox reactivity is not the main driver of the Ce(III) oxidation as Ce(IV) onto goethite. The XANES results showed that 20 % to 50 % of the total Ce bound to goethite was as Ce(IV) and that this linearly increased with the increasing Ce concentration in the solution.

This study obviously assessed an intimate link between both the Ce concentration in solution and the Ce(III) oxidation to Ce(IV) onto goethite. This finding explains the opposite results reported in the literature at high and low $[Ce]_{tot}$ (Denys et al., 2021; Ratié et al., 2020; Yu et al., 2017). The key result highlighted by the study is, therefore, that the concentration of dissolved Ce strongly constraints the Ce redox speciation in solution, i.e., Ce(III) and Ce(IV) aqueous form, leading to spontaneous uptake of Ce(IV) by goethite and more generally by minerals. The Goethite surface seems to stabilize more strongly Ce(IV) than the gibbsite. Therefore, further studies are required for quantifying the effect of the mineral on Ce redox speciation from various Fe oxyhydroxides and other minerals. Moreover, the present findings might apply to other redox sensitive metals exhibiting a poorly soluble oxidation state as compared to other oxidation states, e.g., chromium (Cr(III) vs. Cr(VI)) or tetravalent uranium (U(IV) vs. U(V) or U(VI)), and whose redox speciation might be affected by surface precipitation processes.

Regarding the use of the Ce anomaly as an environmental tracer, except for chemical controlling parameters such as pH (Bau, 1999), other biogeochemical factors can influence the Ce redox behavior: the colloidal fraction (Davranche et al., 2005; Pédrot et al., 2015; 2008), the biological parameters (Ngwenya et al., 2009; Tanaka et al., 2010), and the organic matter (Gangloff et al., 2014; Pourret et al., 2007a). Additionally, to these well-known biogeochemical factors inferring in the use of Ce anomaly, such as an environmental tracer, we, therefore, highlight the role of the Ce soluble concentration and speciation on the amplitude of the Ce anomaly development.

Acknowledgements

This project has received funding from the European Union's Horizon 2020 research and innovation program under the Marie Skłodowska-Curie Grant Agreement N° 857989, by the French ANR project "C-FACTOR" (number ANR-18-CE01-0008) and French CNRS NEEDS project "PREDIRPLUCE". G. Ratié acknowledges the Faculty of Environmental Sciences, Czech University of Life Sciences, Prague (Grant n° IGA FŽP 2020B0025) and the Labex VOLTAIRE, France (10-LABX-0100). Through the support of the GeOHeLiS analytical platform of Rennes University, this publication is also supported by the European Union through the European Regional Development Fund (FEDER), the French Ministry of Higher Education and Research, the French Region of Brittany, and Rennes Metropole. The authors acknowledge the SOLEIL synchrotron for beamtime allocation at the LUCIA beamline (proposal 20200442). We also thank Prof. Karen H. Johannesson for handling our paper.

References

Banik, N.L., Marsac, R., Lützenkirchen, J., Diascorn, A., Bender, K., Marquardt, C.M., Geckeis, H., 2016. Sorption and Redox Speciation of Plutonium at the Illite Surface. Environ. Sci. Technol. 50, 2092–2098. https://doi.org/10.1021/acs.est.5b05129

Banik, N.L., Marsac, R., Lützenkirchen, J., Marquardt, C.M., Dardenne, K., Rothe, J., Bender, K., Geckeis, H., 2017. Neptunium sorption and redox speciation at the illite surface under highly saline conditions. Geochimica et Cosmochimica Acta 215, 421–431. https://doi.org/10.1016/j.gca.2017.08.008

Bao, Z., Zhao, Z., 2008. Geochemistry of mineralization with exchangeable REY in the weathering crusts of granitic rocks in South China. Ore Geology Reviews 33, 519–535.

Bau, M., 1999. Scavenging of dissolved yttrium and rare earths by precipitating iron oxyhydroxide: experimental evidence for Ce oxidation, Y-Ho fractionation, and lanthanide tetrad effect. Geochimica et Cosmochimica Acta 63, 67–77.

Bolanz, R.M., Kiefer, S., Göttlicher, J., Steininger, R., 2018. Hematite (α-Fe2O3)–A potential Ce4+ carrier in red mud. Science of The Total Environment 622, 849–860.

Braun, J.-J., Pagel, M., Muller, J.-P., Bilong, P., Michard, A., Guillet, B., 1990. Cerium anomalies in lateritic profiles. Geochimica et Cosmochimica Acta 54, 781–795.

Brioschi, L., Steinmann, M., Lucot, E., Pierret, M.-C., Stille, P., Prunier, J., Badot, P.-M., 2013. Transfer of rare earth elements (REE) from natural soil to plant systems: implications for the environmental availability of anthropogenic REE. Plant and soil 366, 143–163.

Brookins, D.G., 2018. Aqueous geochemistry of rare earth elements. Geochemistry and mineralogy of rare earth elements 201–226.

Brown, P.L., Ekberg, C., 2016. Hydrolysis of Metal Ions. John Wiley & Sons.

Cao, X., Chen, Y., Wang, X., Deng, X., 2001. Effects of redox potential and pH value on the release of rare earth elements from soil. Chemosphere 44, 655–661.

Chalmin, E., Farges, F., Brown, G.E., 2009. A pre-edge analysis of Mn K-edge XANES spectra to help determine the speciation of manganese in minerals and glasses. Contributions to Mineralogy and Petrology 157, 111–126.

Cheng, W., Kalahroodi, E.L., Marsac, R., Hanna, K., 2019. Adsorption of Quinolone Antibiotics to Goethite under Seawater Conditions: Application of a Surface Complexation Model. Environ. Sci. Technol. 53, 1130–1138. https://doi.org/10.1021/acs.est.8b04853

Davranche, M., Pourret, O., Gruau, G., Dia, A., 2004. Impact of humate complexation on the adsorption of REE onto Fe oxyhydroxide. Journal of Colloid and Interface Science 277, 271–279. https://doi.org/10.1016/j.jcis.2004.04.007

Davranche, M., Pourret, O., Gruau, G., Dia, A., Le Coz-Bouhnik, M., 2005. Adsorption of REE(III)-humate complexes onto MnO2: Experimental evidence for cerium anomaly and lanthanide tetrad effect suppression. Geochimica et Cosmochimica Acta 69, 4825–4835. https://doi.org/10.1016/j.gca.2005.06.005

De Baar, H.J., German, C.R., Elderfield, H., Van Gaans, P., 1988. Rare earth element distributions in anoxic waters of the Cariaco Trench. Geochimica et Cosmochimica Acta 52, 1203–1219.

Denys, A., Janots, E., Auzende, A.-L., Lanson, M., Findling, N., Trcera, N., 2021. Evaluation of selectivity of sequential extraction procedure applied to REE speciation in laterite. Chemical Geology 559, 119954. https://doi.org/10.1016/j.chemgeo.2020.119954

Farges, F., 2005. Ab initio and experimental pre-edge investigations of the Mn K-edge XANES in oxide-type materials. Physical review B 71, 155109.

Flank, A.-M., Cauchon, G., Lagarde, P., Bac, S., Janousch, M., Wetter, R., Dubuisson, J.-M., Idir, M., Langlois, F., Moreno, T., 2006. LUCIA, a micro focus soft XAS beamline. Nuclear Instruments and Methods in Physics Research Section B: Beam Interactions with Materials and Atoms 246, 269–274.

Fonda, E., Andreatta, D., Colavita, P.E., Vlaic, G., 1999. EXAFS analysis of the L3 edge of Ce in CeO2: effects of multi-electron excitations and final-state mixed valence. Journal of Synchrotron Radiation 6, 34–42.

Frey, F.A., 1984. Rare earth element abundances in upper mantle rocks, in: Developments in Geochemistry. Elsevier, pp. 153–203.

Gangloff, S., Stille, P., Pierret, M.-C., Weber, T., Chabaux, F., 2014. Characterization and evolution of dissolved organic matter in acidic forest soil and its impact on the mobility of major and trace elements (case of the Strengbach watershed). Geochimica et Cosmochimica Acta 130, 21–41.

German, C.R., Elderfield, H., 1989. Rare earth elements in Saanich Inlet, British Columbia, a seasonally anoxic basin. Geochimica et Cosmochimica Acta 53, 2561–2571.

Guénet, H., Demangeat, E., Davranche, M., Vantelon, D., Pierson-Wickmann, A.-C., Jardé, E., Bouhnik-Le Coz, M., Lotti, E., Dia, A., Jestin, J., 2018. Experimental evidence of REE size fraction redistribution during redox variation in wetland soil. Science of The Total Environment 631–632, 580–588. https://doi.org/10.1016/j.scitotenv.2018.03.005

Gwenzi, W., Mangori, L., Danha, C., Chaukura, N., Dunjana, N., Sanganyado, E., 2018. Sources, behaviour, and environmental and human health risks of high-technology rare earth elements as emerging contaminants. Science of The Total Environment 636, 299–313. https://doi.org/10.1016/j.scitotenv.2018.04.235

Hiemstra, T., De Wit, J.C.M., Van Riemsdijk, W.H., 1989. Multisite proton adsorption modeling at the solid/solution interface of (hydr)oxides: A new approach: II. Application to various important (hydr)oxides. Journal of Colloid and Interface Science 133, 105–117. https://doi.org/10.1016/0021-9797(89)90285-3

Humphris, S.E., 1984. The mobility of the rare earth elements in the crust, in: Developments in Geochemistry. Elsevier, pp. 317–342.

Janots, E., Bernier, F., Brunet, F., Muñoz, M., Trcera, N., Berger, A., Lanson, M., 2015. Ce (III) and Ce (IV)(re) distribution and fractionation in a laterite profile from Madagascar: insights from in situ XANES spectroscopy at the Ce LIII-edge. Geochimica et cosmochimica acta 153, 134–148.

Jodin, M.-C., Gaboriaud, F., Humbert, B., 2005. Limitations of potentiometric studies to determine the surface charge of gibbsite γ-Al(OH)3 particles. Journal of Colloid and Interface Science 287, 581–591. https://doi.org/10.1016/j.jcis.2005.02.032

Kaindl, G., Schmiester, G., Sampathkumaran, E.V., Wachter, P., 1988. Pressure-induced changes in L III x-ray-absorption near-edge structure of Ce O 2 and Ce F 4: Relevance to 4 f-electronic structure. Physical Review B 38, 10174.

Kanematsu, M., Waychunas, G.A., Boily, J.-F., 2018. Silicate binding and precipitation on iron oxyhydroxides. Environmental science & technology 52, 1827–1833.

Kinniburgh, D.G., Cooper, D.M., 2011. PhreePlot: Creating graphical output with PHREEQC [WWW Document]. URL http://www.phreeplot.org/ (accessed 4.25.20).

Kraemer, D., Tepe, N., Pourret, O., Bau, M., 2017. Negative cerium anomalies in manganese (hydr) oxide precipitates due to cerium oxidation in the presence of dissolved siderophores. Geochimica et Cosmochimica Acta 196, 197–208.

Kulaksız, S., Bau, M., 2011. Rare earth elements in the Rhine River, Germany: first case of anthropogenic lanthanum as a dissolved microcontaminant in the hydrosphere. Environment International 37, 973–979.

Liu, H., Pourret, O., Guo, H., Bonhoure, J., 2017. Rare earth elements sorption to iron oxyhydroxide: Model development and application to groundwater. Applied geochemistry 87, 158–166.

Loges, A., Wagner, T., Barth, M., Bau, M., Göb, S., Markl, G., 2012. Negative Ce anomalies in Mn oxides: the role of Ce4+ mobility during water–mineral interaction. Geochimica et Cosmochimica Acta 86, 296–317.

Luo, T., Xu, J., Cheng, W., Zhou, L., Marsac, R., Wu, F., Boily, J.-F., Hanna, K., 2022. Interactions of Anti-Inflammatory and Antibiotic Drugs at Mineral Surfaces Can Control Environmental Fate and Transport. Environ. Sci. Technol. 56, 2378–2385. https://doi.org/10.1021/acs.est.1c06449

Malterre, D., 1991. L III-edge spectroscopy on cerium-based intermediate-valent compounds. Physical Review B 43, 1391.

Manceau, A., Marcus, M.A., Grangeon, S., 2012. Determination of Mn valence states in mixed-valent manganates by XANES spectroscopy. American Mineralogist 97, 816–827.

Marcus, M.A., Toner, B.M., Takahashi, Y., 2018. Forms and distribution of Ce in a ferromanganese nodule. Marine Chemistry 202, 53–66. https://doi.org/10.1016/j.marchem.2018.03.005

Marsac, R., Banik, N. lal, Lützenkirchen, J., Diascorn, A., Bender, K., Marquardt, C.M., Geckeis, H., 2017a. Sorption and redox speciation of plutonium at the illite surface under highly saline conditions. Journal of Colloid and Interface Science 485, 59–64. https://doi.org/10.1016/j.jcis.2016.09.013

Marsac, R., Banik, N.L., Lützenkirchen, J., Buda, R.A., Kratz, J.V., Marquardt, C.M., 2015a. Modeling plutonium sorption to kaolinite: Accounting for redox equilibria and the stability of surface species. Chemical Geology 400, 1–10. https://doi.org/10.1016/j.chemgeo.2015.02.006

Marsac, R., Banik, N.L., Lützenkirchen, J., Marquardt, C.M., Dardenne, K., Schild, D., Rothe, J., Diascorn, A., Kupcik, T., Schäfer, T., Geckeis, H., 2015b. Neptunium redox speciation at the illite surface. Geochimica et Cosmochimica Acta 152, 39–51. https://doi.org/10.1016/j.gca.2014.12.021

Marsac, R., Davranche, M., Gruau, G., Dia, A., Pédrot, M., Le Coz-Bouhnik, M., Briant, N., 2013. Effects of Fe competition on REE binding to humic acid: Origin of REE pattern variability in organic waters. Chemical Geology 342, 119–127. https://doi.org/10.1016/j.chemgeo.2013.01.020

Marsac, R., Réal, F., Banik, N.L., Pédrot, M., Pourret, O., Vallet, V., 2017b. Aqueous chemistry of Ce(IV): estimations using actinide analogues. Dalton Trans. 46, 13553–13561. https://doi.org/10.1039/C7DT02251D

Massari, S., Ruberti, M., 2013. Rare earth elements as critical raw materials: Focus on international markets and future strategies. Resources Policy 38, 36–43.

McLennan, S.M., 1989. Rare earth elements in sedimentary rocks: influence of provenance and sedimentary processes. Geochemistry and Mineralogy of Rare Earth Elements, Reviews in Mineralogy 21 169–200.

Moffett, J.W., 1990. Microbially mediated cerium oxidation in sea water. Nature 345, 421.

Nakada, R., Takahashi, Y., Tanimizu, M., 2013a. Isotopic and speciation study on cerium during its solid–water distribution with implication for Ce stable isotope as a paleo-redox proxy. Geochimica et Cosmochimica Acta 103, 49–62.

Nakada, R., Tanaka, M., Tanimizu, M., Takahashi, Y., 2017. Aqueous speciation is likely to control the stable isotopic fractionation of cerium at varying pH. Geochimica et Cosmochimica Acta 218, 273–290. https://doi.org/10.1016/j.gca.2017.09.019

Nakada, R., Tanimizu, M., Takahashi, Y., 2013b. Difference in the stable isotopic fractionations of Ce, Nd, and Sm during adsorption on iron and manganese oxides and its interpretation based on their local structures. Geochimica et Cosmochimica Acta 121, 105–119.

Neck, V., Altmaier, M., Müller, R., Bauer, A., Fanghänel, Th., Kim, J.-I., 2003. Solubility of crystalline thorium dioxide. Radiochimica Acta 91, 253–262. https://doi.org/10.1524/ract.91.5.253.20306

Neck, V., Kim, J.I., 2001. Solubility and hydrolysis of tetravalent actinides. Radiochimica Acta 89, 1–16. https://doi.org/10.1524/ract.2001.89.1.001

Ngwenya, B.T., Magennis, M., Olive, V., Mosselmans, J.F.W., Ellam, R.M., 2009. Discrete Site Surface Complexation Constants for Lanthanide Adsorption to Bacteria As Determined by Experiments and Linear Free Energy Relationships [WWW Document]. ACS Publications. https://doi.org/10.1021/es9014234

Nocedal, J., Wright, S., 2006. Numerical optimization. Springer Science & Business Media.

Ohta, A., Kawabe, I., 2001. REE (III) adsorption onto Mn dioxide (δ-MnO2) and Fe oxyhydroxide: Ce (III) oxidation by δ-MnO2. Geochimica et Cosmochimica Acta 65, 695–703.

Parkhurst, D.L., Appelo, C.A.J., 2013. Description of input and examples for PHREEQC version 3: a computer program for speciation, batch-reaction, one-dimensional transport, and inverse geochemical calculations (USGS Numbered Series No. 6-A43), Description of input and examples for PHREEQC version 3: a computer program for speciation, batch-reaction, one-dimensional transport, and inverse geochemical calculations, Techniques and Methods. U.S. Geological Survey, Reston, VA. https://doi.org/10.3133/tm6A43

Pédrot, M., Dia, A., Davranche, M., Bouhnik Le Coz, M., Henin, O., Gruau, G., 2008. Insights into colloid-mediated trace element release at the soil/water interface. Journal of colloid and interface science 325, 187–197.

Pédrot, M., Dia, A., Davranche, M., Gruau, G., 2015. Upper soil horizons control the rare earth element patterns in shallow groundwater. Geoderma 239–240, 84–96. https://doi.org/10.1016/j.geoderma.2014.09.023

Pourret, O., Davranche, M., Gruau, G., Dia, A., 2007a. Organic complexation of rare earth elements in natural waters: Evaluating model calculations from ultrafiltration data. Geochimica et Cosmochimica Acta 71, 2718–2735. https://doi.org/10.1016/j.gca.2007.04.001

Pourret, O., Dia, A., Davranche, M., Gruau, G., Hénin, O., Angee, M., 2007b. Organo-colloidal control on major-and trace-element partitioning in shallow groundwaters: confronting ultrafiltration and modelling. Applied Geochemistry 22, 1568–1582.

Quinn, K.A., Byrne, R.H., Schijf, J., 2007. Sorption of yttrium and rare earth elements by amorphous ferric hydroxide: influence of temperature. Environmental science & technology 41, 541–546.

Quinn, K.A., Byrne, R.H., Schijf, J., 2004. Comparative Scavenging of Yttrium and the Rare Earth Elements in Seawater: Competitive Influences of Solution and Surface Chemistry. Aquatic Geochemistry 10, 59–80. https://doi.org/10.1023/B:AQUA.0000038959.03886.60

Ramos, S.J., Dinali, G.S., de Carvalho, T.S., Chaves, L.C., Siqueira, J.O., Guilherme, L.R.G., 2016a. Rare earth elements in raw materials and products of the phosphate fertilizer industry in South America: Content, signature, and crystalline phases. Journal of Geochemical Exploration 168, 177–186. https://doi.org/10.1016/j.gexplo.2016.06.009

Ramos, S.J., Dinali, G.S., Oliveira, C., Martins, G.C., Moreira, C.G., Siqueira, J.O., Guilherme, L.R., 2016b. Rare earth elements in the soil environment. Current Pollution Reports 2, 28–50.

Ratié, G., Vantelon, D., Pédrot, M., Beauvois, A., Chaouchi, K., Fossé, C., Davranche, M., 2020. Cerium anomalies in riverbanks: Highlight into the role of ferric deposits. Science of The Total Environment 713, 136544. https://doi.org/10.1016/j.scitotenv.2020.136544

Ravel, B., Newville, M., 2005. ATHENA, ARTEMIS, HEPHAESTUS: data analysis for X-ray absorption spectroscopy using IFEFFIT. Journal of synchrotron radiation 12, 537–541.

Rizkalla, E.N., Choppin, G.R., 1994. Chapter 127 Lanthanides and actinides hydration and hydrolysis, in: Handbook on the Physics and Chemistry of Rare Earths. Elsevier, pp. 529–558.

Shields, G., Stille, P., 2001. Diagenetic constraints on the use of cerium anomalies as palaeoseawater redox proxies: an isotopic and REE study of Cambrian phosphorites. Chemical Geology 175, 29–48.

Soldatov, A.V., Ivanchenko, T.S., Della Longa, S., Kotani, A., Iwamoto, Y., Bianconi, A., 1994. Crystal-structure effects in the Ce ${\mathit{L}}_{3}$-edge x-ray-absorption spectrum of ${\mathrm{CeO}}_{2}$: Multiple-scattering resonances and many-body final states. Phys. Rev. B 50, 5074–5080. https://doi.org/10.1103/PhysRevB.50.5074

Stumm, W., Sulzberger, B., 1992. The cycling of iron in natural environments: Considerations based on laboratory studies of heterogeneous redox processes. Geochimica et Cosmochimica Acta 56, 3233–3257. https://doi.org/10.1016/0016-7037(92)90301-X

Takahashi, Y., Manceau, A., Geoffroy, N., Marcus, M.A., Usui, A., 2007. Chemical and structural control of the partitioning of Co, Ce, and Pb in marine ferromanganese oxides. Geochimica et Cosmochimica Acta 71, 984–1008.

Takahashi, Y., Sakami, H., Nomura, M., 2002. Determination of the oxidation state of cerium in rocks by Ce LIII-edge X-ray absorption near-edge structure spectroscopy. Analytica Chimica Acta 468, 345–354. https://doi.org/10.1016/S0003-2670(02)00709-2

Takahashi, Y., Shimizu, H., Usui, A., Kagi, H., Nomura, M., 2000. Direct observation of tetravalent cerium in ferromanganese nodules and crusts by X-ray-absorption near-edge structure (XANES). Geochimica et Cosmochimica Acta 64, 2929–2935.

Tanaka, K., Tani, Y., Takahashi, Y., Tanimizu, M., Suzuki, Y., Kozai, N., Ohnuki, T., 2010. A specific Ce oxidation process during sorption of rare earth elements on biogenic Mn oxide produced by Acremonium sp. strain KR21-2. Geochimica et Cosmochimica Acta 74, 5463–5477. https://doi.org/10.1016/j.gca.2010.07.010

Taylor, S.R., McLennan, S.M., 1988. The significance of the rare earths in geochemistry and cosmochemistry. Handbook on the physics and chemistry of rare earths 11, 485–578.

Tostevin, R., 2021. Cerium Anomalies and Paleoredox. Elements in Geochemical Tracers in Earth System Science. https://doi.org/10.1017/9781108847223

Tostevin, R., Shields, G.A., Tarbuck, G.M., He, T., Clarkson, M.O., Wood, R.A., 2016. Effective use of cerium anomalies as a redox proxy in carbonate-dominated marine settings. Chemical Geology 438, 146–162.

Vantelon, D., Trcera, N., Roy, D., Moreno, T., Mailly, D., Guilet, S., Metchalkov, E., Delmotte, F., Lassalle, B., Lagarde, P., 2016. The LUCIA beamline at SOLEIL. Journal of synchrotron radiation 23, 635–640.

Xu, J., Marsac, R., Wei, C., Wu, F., Boily, J.-F., Hanna, K., 2017. Co-binding of Pharmaceutical Compounds at Mineral Surfaces: Mechanistic Modeling of Binding and Cobinding of Nalidixic Acid and Niflumic Acid at Goethite Surfaces. Environmental Science & Technology 51, 11617–11624. https://doi.org/10.1021/acs.est.7b02900

Yu, C., Drake, H., Mathurin, F.A., Åström, M.E., 2017. Cerium sequestration and accumulation in fractured crystalline bedrock: the role of Mn-Fe (hydr-) oxides and clay minerals. Geochimica et Cosmochimica Acta 199, 370–389.

Zhong, S., Seltmann, R., Qu, H., Song, Y., 2019. Characterization of the zircon Ce anomaly for estimation of oxidation state of magmas: a revised Ce/Ce* method. Mineralogy and Petrology 113, 755–763.

Graphical abstract

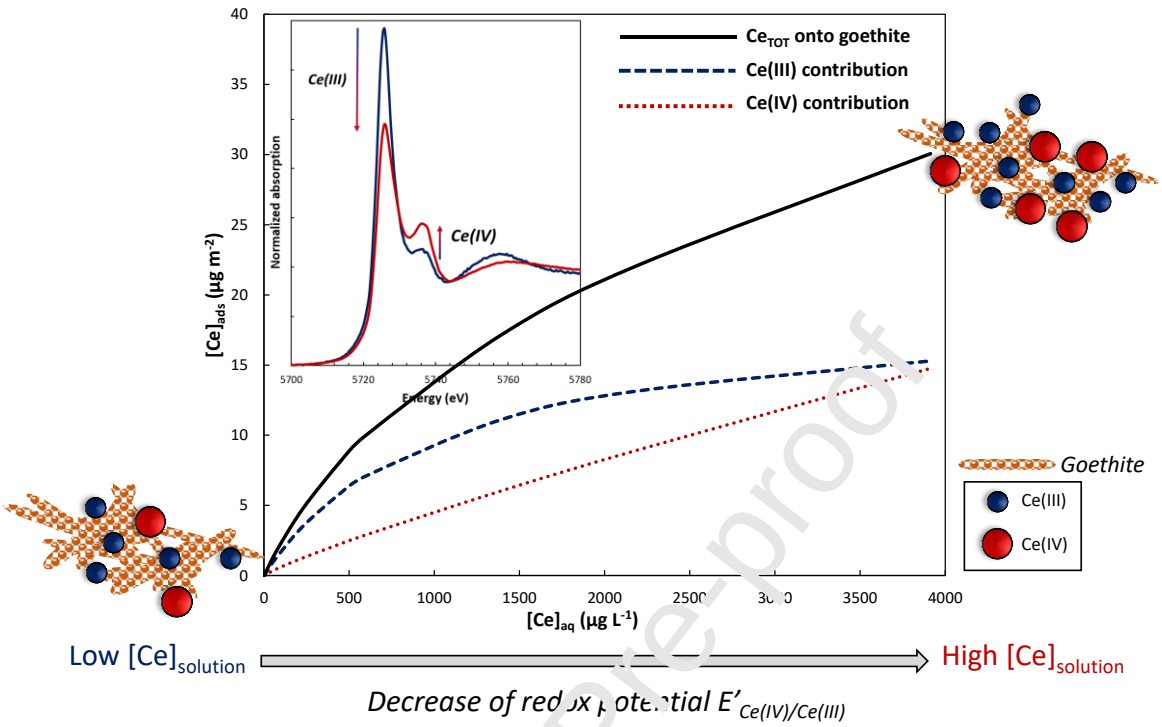

Declaration of interests

☒ The authors declare that they have no known competing financial interests or personal relationships that could have appeared to influence the work reported in this paper.